Dalton Transactions

PAPER

View Article Online
View Journal | View Issue

Cite this: *Dalton Trans.*, 2026, **55**, 279

Green synthesis of oxygen-vacancy-rich NiV-LDH photocatalysts for the enhancement of photocatalytic H_2O_2 production and Cr(VI) detoxification

Preeti Prabha Sarangi, Jyotirmayee Sahu, Rasan Kumar Giri and Kulamani Parida *

This work represents a comprehensive investigation into the synthesis, morphology, and electronic structure of NiV-layered double hydroxide (NiV-LDH) nanoflakes for enhanced photocatalytic applications. Ultrathin NiV-LDHs with varying Ni and V ratios were successfully synthesized *via* a green reflux method. The presence of oxygen vacancies (O_v) and the high surface area of NV-2 synergistically tuned the electronic structure and facilitated the charge segregation by trapping the photogenerated electrons (e^-), suppressing their rapid recombination with holes (h^+), and leading to an enhanced catalytic efficiency. Consequently, the optimized NV-2 photocatalyst exhibited the highest photocatalytic hydrogen peroxide (H_2O_2) production of 1152.5 ± 38.2 μmol g^{-1} h^{-1} from O_2 in an ethanol–water solution and 81.5% of Cr(VI) reduction in 2 h under visible light irradiation while demonstrating excellent stability for up to five cycles. In addition, the NV-2 exhibited a solar to chemical conversion efficiency rate (SCC) of 0.089% for photocatalytic H_2O_2 production. The scavenger testing of NV-2 implied that the production of H_2O_2 followed a direct two-electron pathway. Likewise, the Cr(VI) reduction by NiV-LDHs followed pseudo-first order kinetics. The low intense photoluminescence spectra, highest photocurrent density, smallest arc radius in the impedance spectra of NiV-LDHs, along with the Mott–Schottky (MS) analysis, led to an understanding of the mechanistic aspects of their photocatalytic activities. This work highlights a cost-effective, eco-friendly strategy for developing defect-engineered LDH materials with promising potential for environmental remediation and sustainable photocatalysis.

Received 10th September 2025,
Accepted 18th November 2025

DOI: 10.1039/d5dt02178b

rsc.li/dalton

Introduction

The 21st century is primarily concerned with rapid population growth and excessive industrialisation, which have led to energy crisis and environmental pollution.[1,2] The excessive use of fossil fuels adversely affects the environment and earth through carbon dioxide emissions and other hazardous chemicals. Nowadays, there is an urgent need for a sustainable, low-energy synthesis protocol owing to the growing need for clean energy and the scarcity of conventional production approaches. In this regard, photocatalysis has emerged as a promising alternative, capable of harnessing renewable solar energy into valuable chemical fuels such as H_2, NH_3, CH_4, and H_2O_2 over semiconductor surfaces to escalate global energy requirements. Among the various alternatives, H_2O_2 is a highly adaptable, clean oxidizing agent that produces only water and oxygen as byproducts. It is a critical renewable energy resource, extensively employed in disinfection, sterilisation, cleaning, bleaching, wastewater treatment, and organic synthesis. It is safe to store, convenient to transport in aqueous form, and functions both as a reducing and oxidizing agent in a single-compartment fuel cell. However, the traditional anthraquinone auto-oxidation route, dominated in the industrial H_2O_2 production, is associated with toxic organic solvents and a high-energy multi-step synthesis protocol, and therefore, it is unfavourable for small-scale application. In this regard, understanding the reaction mechanism, extending the lifespan of the photocatalyst, and improving the efficiency of the photocatalytic yield remain fascinating challenges of modern photocatalysis. Overcoming these barriers requires a unique, sustainable and energy-saving approach. With respect to the high energy consumption of the traditional anthraquinone route for H_2O_2 generation, photocatalytic H_2O_2 synthesis from O_2 *via* a $2e^-$ process, *i.e.*, the oxygen reduction reaction (ORR) ($O_2 + 2e^- + 2H^+ \rightarrow H_2O_2$), appears to be an energy-saving, green and stable alternative.[3,4]

Centre for Nano Science and Nano Technology, ITER, Siksha 'O' Anusandhan Deemed to be University, Bhubaneswar, Odisha, 751030, India.
E-mail: sarangipreetiprabha9178@gmail.com, jsahu962016@gmail.com, rasankumargiri@gmail.com, kulamaniparida@soa.ac.in, kulamaniparida@soauniversity.ac.in, paridakulamani@yahoo.com; Fax: +91-674-2350642; Tel: +91-674-2351777, +91-9776645909

Recent studies have revealed that photocatalytic H_2O_2 production offers dual functionality in eradicating the necessity for external oxidants, enabling *in situ* H_2O_2 production alongside pollutant deprivation. For instance, Ghoreishian *et al.* designed a solar-driven Bi_2S_3@CdS/RGO S-scheme-based ternary heterostructure that was utilised for simultaneous photocatalytic H_2O_2 generation and Cr(VI) reduction towards energy and environment sustainability.[5] In a similar study, Ghoreishian and team presented an efficient visible-to-NIR-induced B-C_3N_4@Bi_2S_3 hybrid heterostructure that exhibited photocatalytic H_2O_2 generation and pollutant detoxification, highlighting the significance of interfacial charge transfer and defect engineering in enhancing H_2O_2 selectivity and stability.[4] These developments collectively affirm the successful integration of photocatalytic H_2O_2 generation for efficient pollutant removal and solar-to-chemical conversion.[6]

Over the past few decades, the worsening of heavy metal pollution has emerged as a critical environmental issue owing to its heavy threat to human health and environmental safety. Among various heavy metal ions, including Cd(II), Pb(II), Hg(II), As(III/V), and Cr(VI), hexavalent chromium is one of the most prevalent and toxic contaminants, mainly due to its extensive usage in industries such as electroplating, leather tanning, and mining. Conventional methods employed for Cr(VI) removal from wastewater include chemical precipitation, coagulation, filtration, adsorption, and biological treatments. Very recently, the transformation of Cr(VI) to the less toxic Cr(III) has received much attention owing to its cost-effectiveness, environmental compatibility and the simplicity of the method.[7,8]

Different photocatalysts, such as metal oxides,[9,10] metal sulfides, graphitic carbon nitrides,[11–13] layered double hydroxides,[14] and different metal organic frameworks,[15] have been explored to catalyse the production of H_2O_2, and the decontamination of Cr(VI) to Cr(III), among which transition metal-based layered double hydroxide materials have attracted considerable attention.[7,16–19] LDHs, structural analogues of hydrotalcite, consist of positively charged brucite-like metal hydroxide layers containing octahedral $M^{2+}/M^{3+}(OH)_2$ units residing over edges, whose charges are neutralised by interlayer anions. These materials have gained significant attention in photocatalysis due to their tunable metal cation composition, appropriate bandgap, exchangeable intercalated anion tendencies, compositional flexibility, cost-effectiveness, and potential for precise interfacial tuning when integrated with other suitable semiconductors.[20–22] Among transition-metal-based LDHs, NiV-LDH has recently emerged as an effective photocatalyst owing to its moderate surface area, optimal band gap energy, and favourable optoelectronic properties. Furthermore, the enhanced photocatalytic performance of NiV-LDHs is largely attributed to efficient charge transfer facilitated by the partially filled or vacant 3d orbitals of Ni and V.[23] Nonetheless, limited solar light absorption, low quantum efficiency, insufficient active sites, sluggish charge transport and rapid recombination still hinder their overall photocatalytic activity. To address these limitations, strategies like nanostructure engineering, elemental doping, defect (vacancy) generation, and heterojunction construction have been widely adopted. In this context, NiV-LDH has attracted much attention due to its specific surface area (SSA) and structural diversity. In particular, the porous structure of the material plays a key role, acting as an active center throughout the photocatalytic process.

Considering that the LDHs have a broad light absorption capacity, and it is easy to induce defects such as O_v, we have designed the carbonate-intercalated NiV-LDH following a reflux method. For achieving the optimal conditions, the reflux reaction parameters of NiV-LDH have been explored by adjusting the ratio of Ni : V to 2 : 1, 3 : 1, and 4 : 1, which have been correspondingly termed as NV-2, NV-3, and NV-4. Thus, the optimized NV-2 photocatalyst demonstrated significantly higher yield than the other two synthesized catalysts. Further, comprehensive studies on the photoluminescence and electrochemical properties of NiV-LDHs were conducted, which elucidated the slowest exciton recombination rate and highest charge carrier separation efficiency of NV-2, showing the optimum photocatalytic H_2O_2 production and Cr(VI) reduction. The unique morphological architecture with the nanoflake structure accelerated the charge transfer phenomena. It exhibited outstanding long-term stability for up to five cycles. Moreover, the efficiency was facilitated by the in-depth understanding of the exciton transfer on the surface of the photocatalyst. The time-resolved photoluminescence and Bode phase plot of the as-synthesized catalysts demonstrated the lifespan of their excited electrons, which improved the photocatalytic performances.

Results and discussion

The NV was fabricated *via* a facile reflux method, as illustrated schematically in Fig. 1a. The crystallite phase component of the prepared photocatalyst was detected using X-ray diffraction (XRD). Fig. 1b shows the XRD spectra of NV photocatalysts, in which the systematic variation in XRD patterns can be observed due to different amount of VCl_3 incorporation over the $NiCl_2$ matrix. The peaks for the NV specimen were detected at the 2θ angles of 11.28°, 22.86°, 35.12°, 39.56°, and 47.22°, which are associated with the (003), (006), (009), (012), and (110) planes, respectively, implying that NV exists in the rhombohedral phase (JCPDS-52-1627), having the space group *R*3*m*. The lattice constants of NV were found to be $a = b = 3.08$ and $c = 23.6$. Interestingly, significant broadening of the peak width and reduction in the diffraction peak intensity along the (003), (006), (009), (012), and (110) crystal planes were observed for NV-3 and NV-4 with increasing amounts of $NiCl_2$ in the matrix, as compared to NV-2. The Williamson–Hall (W–H) plot was applied to observe the variation in crystallite size for the prepared NV samples (Fig. S1a–c). The estimated results showed that the average crystallite size (D) was 4.86, 5.03, and 6.08 nm for NV-2, NV-3, and NV-4, respectively. Average lattice constants and micro strain of NV-2, NV-3, and NV-4 were also calculated from the PXRD data and are represented in Table S1. The

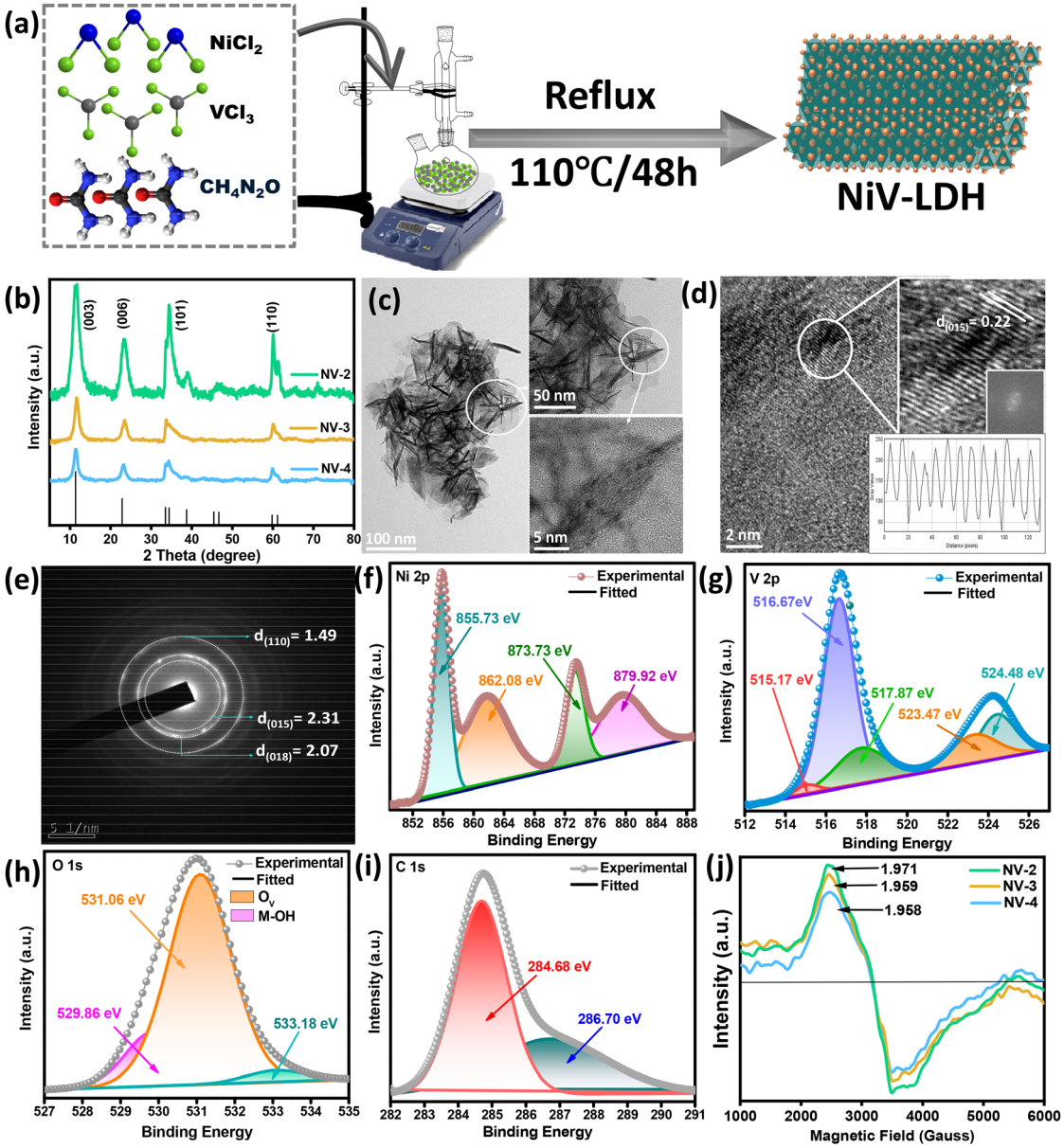

Fig. 1 (a) Schematic of the synthesis of NV nanoflakes by the reflux method. (b) XRD data of NV-2, NV-3, and NV-4. (c) Different magnified TEM images of NV-2 nanoflakes. (d) HRTEM pattern with lattice fringe analysis and (e) the corresponding SAED pattern. XPS and deconvoluted spectra of (f) Ni 2p, (g) V 2p, (h) O 1s, and (i) C 1s. (j) *Ex situ* EPR signals of the NV-2, NV-3, and NV-4 photocatalysts.

interlayer spacing and delocalization density for the (003) plane are also illustrated in Table S1.[17,24] Further insights into the surface morphology of NV-2 were gained using scanning electron microscopy (SEM) and field emission scanning electron microscopy (FESEM) technologies. As portrayed in Fig. S2a, the hierarchical NV-2 maintained the flake architecture.[25] The FESEM images of NV-2 revealed a uniform distribution of sheet-agglomerated flower-like structures. From Fig. S2b, the FESEM colour mapping, along with the atomic and wt%, indicated that the Ni and V elements were homogenously distributed in the NV-2 catalyst. As detected from high-resolution transmission electron microscopy (HRTEM), a partially amorphous structure exists in the NV specimen. Notably, numerous petal-like structures were detected, which can be attributed to the NV-2 catalyst as displayed in Fig. 1c. Further examination of the HRTEM image (Fig. 1d) unveiled a lattice spacing of 0.22 nm corresponding to the (015) crystallographic plane, thus confirming the successful synthesis of the NV-2 photocatalyst. The SAED pattern of NV-2 depicted in Fig. 1e brings out the polycrystalline nature of NV-2 with *d*-spacings of 1.49, 2.07, and 2.31 nm for the (110), (015), and (018) lattice planes, respectively.[21,22] The particle size distribution histogram (Fig. S2c) was obtained by measuring selected particle sizes from the corresponding SEM image. The average particle

size (d_{SEM}) for NV-2 is about 102.53 nm. These findings compellingly verify the successful formation of the NV-2 photocatalyst.

X-ray photoelectron spectroscopy (XPS) was used to analyse the surface chemical states of the NV-2 catalyst. The XPS survey spectra confirmed the presence of all the elements of the NV photocatalyst (Fig. S2d). The deconvoluted spectra of Ni 2p (Fig. 1f) exhibit two binding energy peaks located at 855.73 and 873.73 eV, attributed to Ni $2p_{3/2}$ and $2p_{1/2}$ spin–orbit coupling, respectively. Ni 2p contributes 16.28% of the atomic composition, and the difference between Ni $2p_{3/2}$ and Ni $2p_{1/2}$ is 18 eV, revealing the successful formation of Ni^{2+} oxidation states. Again, the high-resolution XPS spectra of V 2p (Fig. 1g) deconvoluted into V $2p_{3/2}$ and $2p_{1/2}$ were broadened with multiple peaks, due to spin–orbit splitting. The XPS deconvoluted spectra of V 2p reveal three clear peaks indexed at 515.09, 516.67, and 517.72 eV attributed to the +3, +4, and +5 oxidation states of V $2p_{3/2}$, respectively. Two peaks detected at 523.24 and 524.72 eV represent the V $2p_{1/2}$ energy levels. The binding energy difference between V $2p_{3/2}$ and $2p_{1/2}$ is 8.15 eV.[25,26] The O 1s spectrum exhibited the highest atomic percentage of 54.02%, possibly arising from OH^- species within the layered double hydroxide structure (Fig. 1h).[27,28] The peak detected at 529.86 eV indicates that the O species merged with the metal hydroxyl group (M–OH), and 533.18 eV was attributed to M–O. The peak observed at 531.06 eV was attributed to O_v, revealing the presence of oxygen defect sites in the photocatalyst.[29] As displayed in Fig. 1i, C 1s showed two deconvoluted peaks corresponding to the non-oxygenated (C–C) rings at 284.68 eV and the carboxyl carbons (C–C═C) at 286.70 eV. Fig. S2e shows the atomic percentage of all the elements present in NV-2, further confirming the successful formation of the catalyst specimen. To support the presence of vacancies and the paramagnetic behaviour of the catalyst, electron paramagnetic resonance spectroscopy (EPR) was conducted at room temperature. As exhibited in Fig. 1j, the g values at 1.971, 1.959, and 1.958, corresponding to NV-2, NV-3, and NV-4, were respectively indexed to O_v.[30] The possible reason behind the decrease in the EPR intensity of NV-3 and NV-4 as compared to that in NV-2 might be the coverage of O_v sites by Ni dispersed over the surface.[26] The NV-4 and NV-3 possess stronger metal support interactions, which may be attributed to more Ni being dispersed over the surface, preventing the generation of O_v. This suggests that more unpaired electrons are available at the NV-2 catalyst for resonance, which, in turn, results in a stronger EPR signal than the other two catalysts.

Next, we examined the functional groups present in the NV material using FTIR spectroscopy (Fig. S3a). The peaks in the 550–1030 cm^{-1} region were due to the M–O, O–M–O and M–O–M (M = Ni/V) lattice stretching and bending vibrations. The peak at 843 cm^{-1} indicates the presence of V–O stretching vibrations. The peaks at ~670 and 1374 cm^{-1} symbolize the stretching vibrations of intercalated carbonates, which were also revealed by the (003) XRD peak.[31,32] The absorption peak at 1636 cm^{-1} was attributed to the bending vibration mode of water molecules. The broad absorption peak of NV, starting from 3200 cm^{-1} to 3550 cm^{-1}, was due to the stretching vibrations of the OH-group present in the LDH lattice.[27] The chemical bonding state and structural defects were examined using Raman Spectroscopy to further validate the NV-2 photocatalyst formation.[33,34] As depicted in Fig. S3b, the characteristic peak observed in the range of 100–900 cm^{-1} signifies the M–O (M = Ni/V) and O–M–O stretching vibrational modes. In particular, multiple broad peaks were observed at 164.57, 242.84, 343.36, 467.98, and 530.29 cm^{-1}, attributed to the stretching vibration of the V–O bond.[30] Specifically, the main intense peak observed at 851.23 cm^{-1} was attributed to the V–O bond vibration, which also matches the FTIR results ($n_{(V-O)}$ = 843 cm^{-1}). The 1383.52 cm^{-1} band was specifically attributed to the CO_3^{2-} ion in the NV LDH materials. The peak at 1649 cm^{-1} symbolizes the bending mode of interlayer water molecules. These results indicate the successful fabrication of NV samples.

The SSA of the catalyst was explored using the Brunauer–Emmett–Teller (BET) isotherm. The SSA of NV-2 was estimated to be 148.2 $m^2\ g^{-1}$ and the average pore diameter was 3.4 nm. Fig. S3c exemplifies the N_2-adsorption–desorption of the NV-2 catalyst. The catalyst showed a type IV adsorption isotherm according to the Brunauer–Deming–Deming–Teller (BDDT) classification, suggesting the presence of a porous structure, which may be attributed to capillary condensation. Further, the NV-2 showed an H3 hysteresis loop, suggesting the existence of slit-shaped pores derived from the aggregated particles, along with a narrow pore size between 2–10 nm, as depicted by the BJH plot (inset Fig. S3c).

Bandgap calculation

The energy level alignments of the photocatalysts were investigated using UV-vis absorption, and the M–S plots were analyzed. The light-absorption ability and band gap of the as-prepared catalysts were analyzed using UV-vis diffuse reflectance spectra (UV-vis DRS). The absorption peaks due to the d–d transitions of Ni^{2+} and V^{3+} were found in the visible region, covering the wavelength from 200 nm to 800 nm at room temperature, and are represented in Fig. 2a.[35] The catalysts exhibited two absorption maxima (λ_{max}) at around 330 nm, attributed to the ligand-to-metal charge transfer transition.[36] The wide UV-vis absorption between 200 and 600 nm is ascribed to the d–d transitions ($^6A_{1g}(S)/^4T_{2g}$, $^4E_{2g}(D)$ and $^6A_{1g}(S)/^4E_g$, $A_{1g}(G)$) representing the V atom coordination. Another absorption peak observed around 650–750 nm was ascribed to the spin-forbidden transition ($^3A_{2g}(F)/^1T_{2g}(D)$) and the spin-allowed transition ($^3A_{2g}(F)/^3T_{1g}(P)$), corresponding to octahedral Ni in the NV layer.[25] Moreover, the bandgap of the as-prepared catalyst was evaluated based on the Tauc plot (Fig. S4a) and eqn (S1). The direct optical values of NV-2, NV-3, and NV-4 were determined to be 1.58, 1.46, and 1.23 eV, respectively.[37] To calculate the width of the tail of localised defect states within the bandgap, Urbach energy (E_u) was considered. When a photocatalyst is exposed to light of a specific wavelength, the defect states capture the excited electrons,

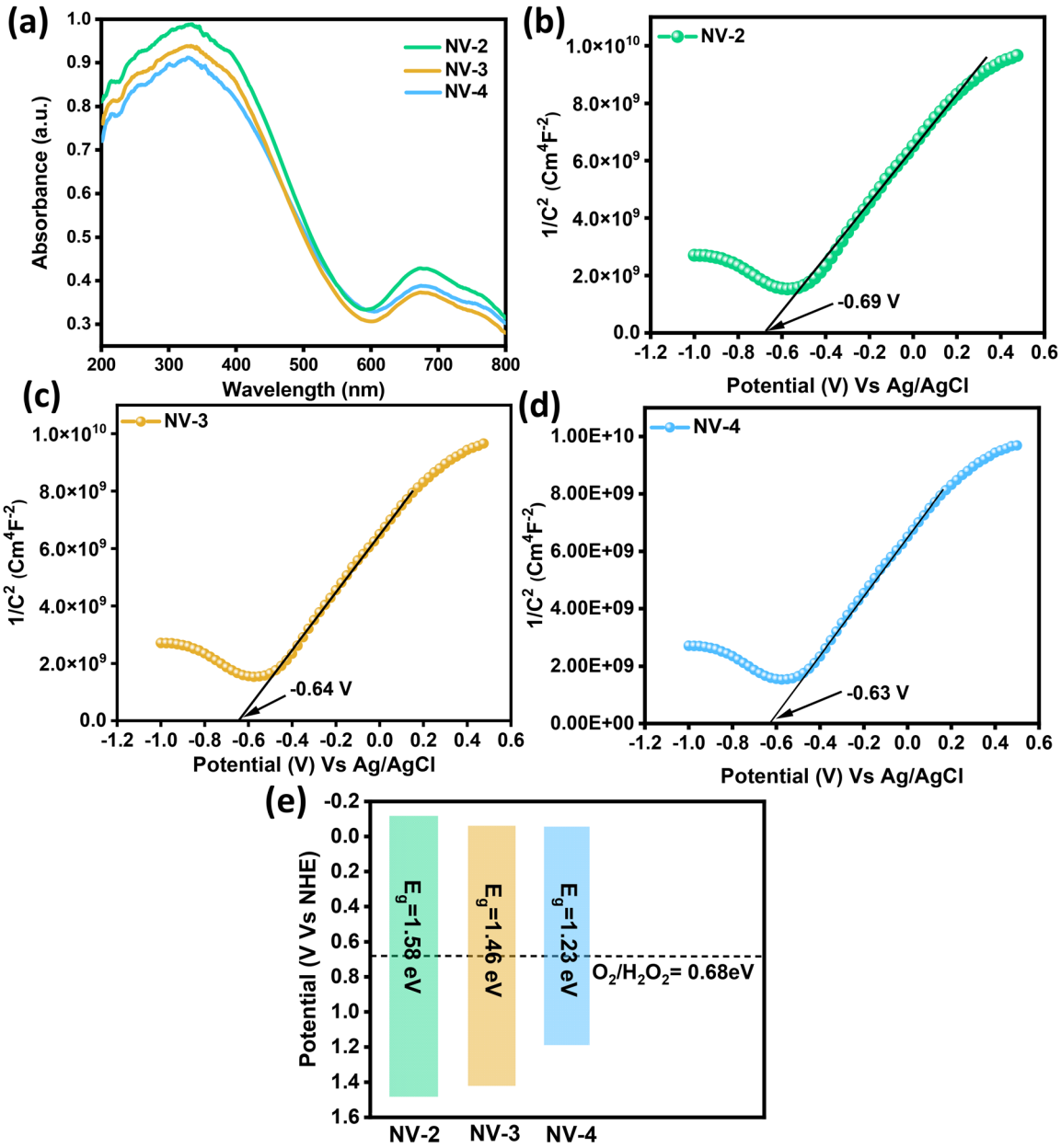

Fig. 2 (a) UV-vis absorption of NV photocatalysts. M–S analysis of (b) NV-2, (c) NV-3, and (d) NV-4. (e) Band edge potential of NV catalysts.

hindering their direct transition. These defect states give rise to an absorption tail in the spectrum, known as the Urbach tail, which is linked to the E_u. The E_u is determined from the reciprocal of the slope of the linear fit in the region below the optical bandgap, and the obtained values are listed in Table S2.[38] From the table, it can be seen that NV-2 results in an increase in Urbach energy, which can increase the O_v centers in the system as compared to those of the NV-3 and NV-4 (Fig. S4b–d). This may be due to the introduction of multivalent vanadium, which can improve electronic activity, indicating that the ultrathin NV-2 has excellent visible light photocatalytic activity.[39] Further, as shown in Fig. 2a, combined with UV analysis, the M–S curves show that all the catalysts are n-type semiconductors. The flat-band potentials (E_{fb}) of NV-2, NV-3, and NV-4 were −0.12, −0.06, and −0.05 V, respectively (Fig. 2b–d). As a result, the E_{VB} values for NV-2, NV-3, and NV-4 semiconductors were determined to be approximately 1.46, 1.41, and 1.19 eV, respectively, using the equation $E_{VB} = E_{CB} + E_g$ (Fig. 2e). Hence, the prepared catalysts meet the thermodynamic requirements for H_2O_2 production.

To further elucidate the influence of O_v and NV-2 nanoflakes on the separation and transfer of photogenerated carriers, the influence was first investigated using PL and TR-PL spectroscopy. As shown in Fig. 3a, the PL of NV-2 exhibited the lowest PL intensity among all samples, indicating that O_v effectively inhibited the recombination of photogenerated exciton

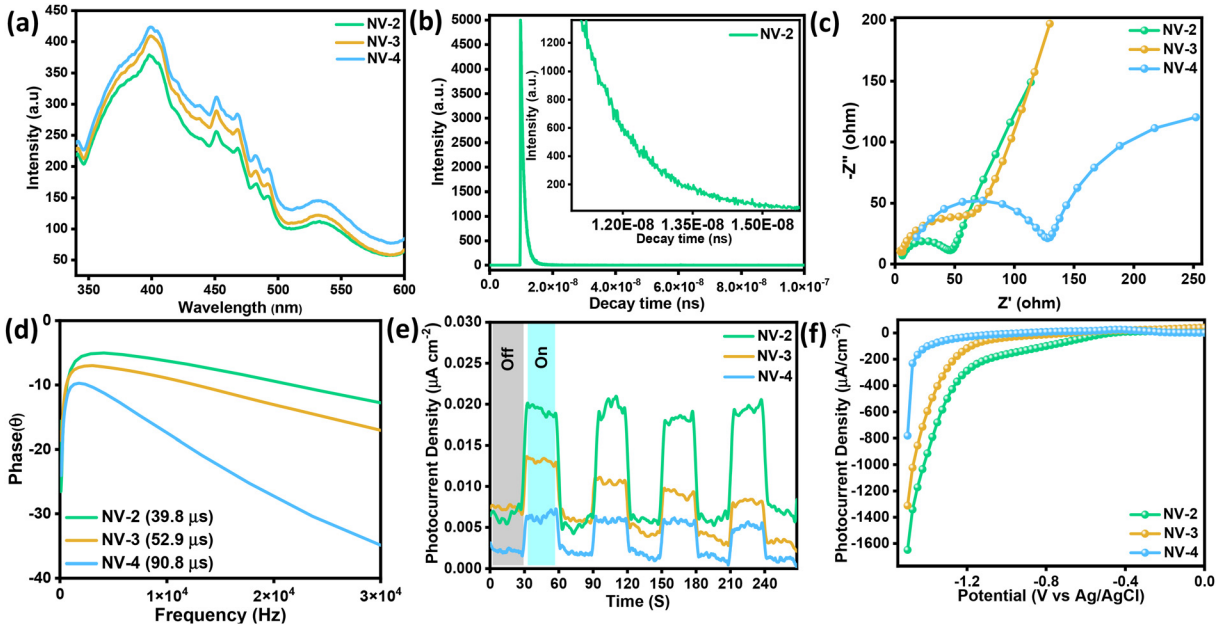

Fig. 3 (a) PL emission spectral analysis of the NV photocatalysts with an excitation wavelength of 320 nm. (b) TR-PL spectra of the NV-2 sample. (c) Nyquist plots, (d) Bode phase plots, (e) transient-photocurrent density, and (f) LSV plots of NV samples using 0.1 M Na_2SO_4 aq. solutions.

pairs. Correspondingly, the TRPL spectra of the least intense catalyst were recorded and fitted based on the biexponential decay eqn (S2). The average carrier lifespan ($\tau_{avg.}$) of NV-2 was calculated to be 1.04 ns. The rapid decay of τ_{avg} suggested that the accumulation of O_v and NV-nanoflakes facilitated the effective transfer of photogenerated carriers (Fig. 3b).[40] Fig. 3c shows that the radius of the NV-2 is smaller than that of NV-3 and NV-4, which indicates that the electron transfer on the surface of NV-2 is easier than that on NV-3 and NV-4. The existence of O_v greatly affects the electron transfer capability, leading to the enhancement of catalytic activity. The electron trapping sites and surface O_v, which modulate the coordination structure and electronic states of the surface adsorbates, facilitate the formation of reactive species that enhance the charge transfer ability on the surface of NV-2, attributed to abundant O_v.[41,42] As displayed in Fig. 3d, we analysed the properties of the Bode plot to evaluate the life span of the generated electrons. The results of the Bode experiment were calculated and recorded in Table S3. It was observed that NV-2 exhibited the longest electron lifetime as compared to NV-3 and NV-4, which improved the photocatalytic activity. To examine the separation and accumulation of the photogenerated charge carriers, the transient photocurrent was analysed. As shown in Fig. 3e, the NV-2 exhibited the highest photocurrent response compared to NV-3 and NV-4, indicating effective electron mobility and the highest separation efficiency of the photogenerated charge carriers in the NV-2 sample.[42] The linear sweep voltammetry (LSV) plot revealed the superior catalytic performance and the cell voltage necessary to attain current densities of the NV electrodes. Fig. 3f shows that at a scan rate of 50 mV s^{-1} in the electrolyte solution (0.01 M) of Na_2SO_4, the as-prepared NV samples exhibited cathodic current under light irradiation. In comparison to NV-3 and NV-4, the NV-2 catalyst achieved a better current density of −3382.71 µA cm^2, which led to the highest exciton generation ability and enhanced the charge carrier transfer.[43,44] Moreover the obtained overpotential values for NV-3 and NV-4 were −1311.38 and −781.948 µA cm^2, respectively.

Photocatalytic activity

Photocatalytic H_2O_2 production. The photocatalytic H_2O_2 production capabilities of the as-prepared NV catalysts were studied first in water and O_2 environments under visible light irradiation ($\lambda \geq 400$ nm), and were determined by the iodometric method. The initial pH of the reaction solution was 7.3. The NV-2 photocatalyst showed superior photocatalytic H_2O_2 performance with a rate of 1152.5 ± 38.2 µmol g^{-1} h^{-1} in 60 min as compared to NV-3 (826.72 ± 31.24 µmol g^{-1} h^{-1}) and NV-4 (698.23 ± 28.36 µmol g^{-1} h^{-1}) (Fig. 4a); this is due to the well-tuned proportions of Ni and V, resulting in differences in SSA and O_v.[45,46]

Next, the reaction kinetics of H_2O_2 production over NV catalysts were studied. The formation rate constants (K_f) for NV-2, NV-3 and NV-4 catalysts were detected to be 19.2, 13.77, 11.64 µmol h^{-1}, while H_2O_2 decomposition rate constants (K_d) for the catalysts were 18.1 × 10^{-4} h^{-1}, 71.1 × 10^{-4} h^{-1}, and 106.1 × 10^{-4} h^{-1}, respectively, satisfying the eqn (S3) and (S4) as depicted in Fig. 4b. Additionally, Fig. S5a displays the lower H_2O_2 decomposition rate of NV-2 as compared to pure H_2O_2 solution. As shown in Fig. 4c, the decomposition value of NV-2 gradually decreased with an increase in Ni concentration,

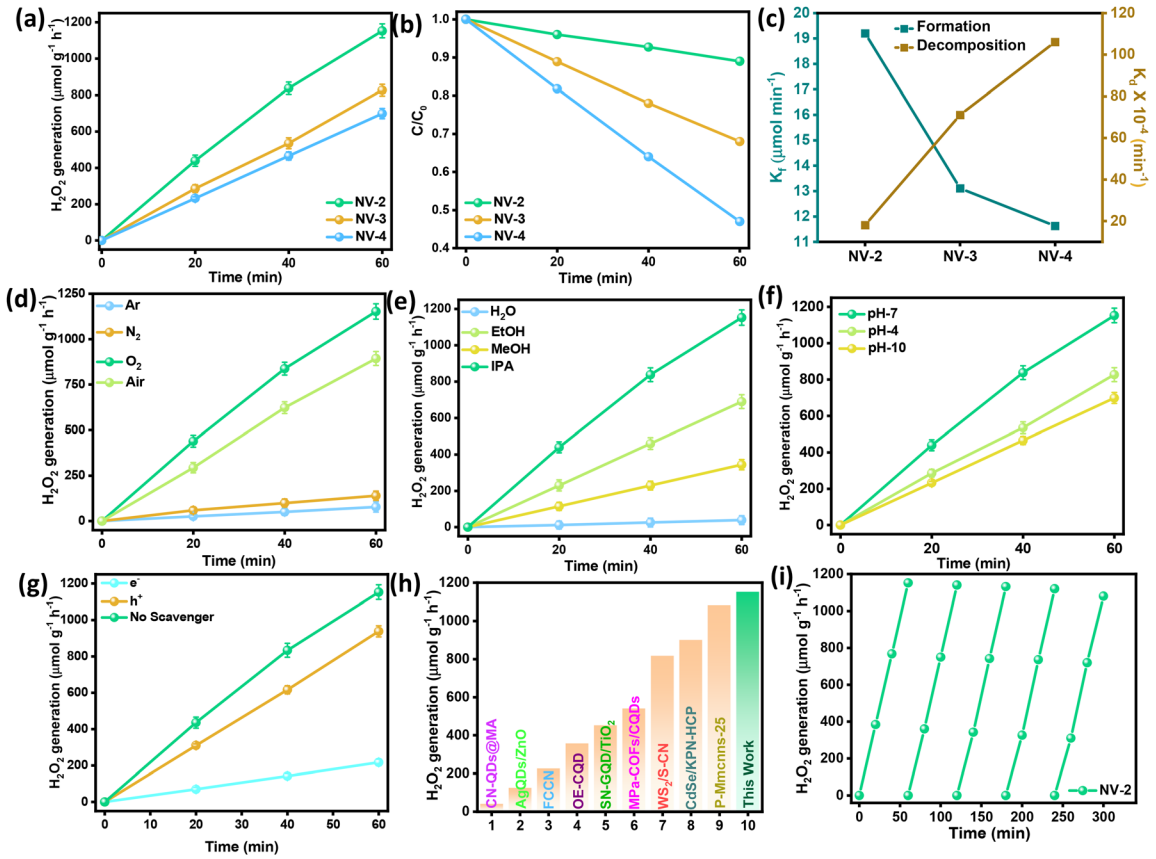

Fig. 4 (a) Photocatalytic H_2O_2 production performance under visible light irradiation. (b) Photocatalytic decomposition of NV photocatalysts. (c) K_d and K_f values for the photocatalytic production of H_2O_2 during 1 h of catalytic process of all the samples. (d) H_2O_2 production in different atmospheres. (e) Photocatalytic H_2O_2 production over different hole scavengers. (f) Photocatalytic H_2O_2 production under different pH values. (g) Different scavenging tests. (h) Comparison of the photocatalytic H_2O_2 production by different photocatalysts. (i) Stability testing of the NV-2 catalyst during the H_2O_2 production.

where the optimal ratio of the Ni and V (2 : 1) content exhibited the largest K_f while maintaining the lowest K_d value, which greatly improved the H_2O_2 production rate. Controlled experiments under different atmospheres of NiV LDHs were examined and are illustrated in Fig. 4d. Notably, the NV-2 catalyst exhibited the highest yield under an O_2 atmosphere, while in an air atmosphere, the yield was comparatively decreased. Further, the photocatalytic H_2O_2 production rate was reduced in the N_2 and Ar atmospheres, emphasizing that an O_2-rich atmosphere significantly promoted the H_2O_2 productivity under visible light irradiation.[47–50] As displayed in Fig. 4e, in the absence of sacrificial reagents, the NV-2 catalyst showed an impressive H_2O_2 production rate of 1152 μmol g^{-1} h^{-1}. NV-2 exhibited the highest yield after the introduction of 10% of IPA, which could be attributed to a better dispersity of the catalyst and hence a greater utilization of the photoexcited charge carriers. NV-2 maintained efficient H_2O_2 production performance over a wide pH range. The optimal pH value for the generation of H_2O_2 was achieved at pH = 7 because of the concentration of protons provided by the IPA solution. In an acidic medium (pH = 4), the catalytic efficiency decreased due to the occurrence of competitive H_2 evolution.[7] A small amount of H_2O_2 was also produced in alkaline medium (pH = 10) as compared to pH = 7 (Fig. 4f). In order to further explore the photocatalytic mechanism of H_2O_2 generation, scavenger-quenching tests were conducted. $AgNO_3$ and citric acid were applied to quench e^-, and h^+, respectively (Fig. 4g). The reactive species quenching experiment indicated that the H_2O_2 generation rate of NV-2 was suppressed by the addition of $AgNO_3$ to the reaction system; however, the H_2O_2 yield was increased after the addition of IPA, which suggested that e^- is the major reactive species involved in the H_2O_2 production through a direct $2e^-$ pathway. Furthermore, NV-2 demonstrated superior performance as an excellent photocatalyst for H_2O_2 production, as shown in Fig. 4h, and the details, including photocatalysts and reaction parameters, are presented in Table S4.[51–53] Notably, the H_2O_2 generation rate of NV-2 was optimised to 1152.5 μmol g^{-1} h^{-1}; no significant decrease in H_2O_2 production was observed after 5 cycles, as illustrated in Fig. 4i. For further confirmation, the XRD of NV-2 after reaction was analysed and no significant changes were noticed, even after the photocatalytic performance (Fig. S5b).

Photocatalytic Cr(VI) reduction. The photocatalytic hexavalent Cr(VI) reduction by the as-synthesized samples was per-

formed under LED light illumination, as shown in Fig. 5a. At first, a blank experiment was performed in the dark and in the absence of a photocatalyst, which demonstrated no significant reduction of Cr(VI), confirming light and the photocatalyst as indispensable factors for photocatalytic Cr(VI) reduction. The photocatalytic activity was performed in the dark for the first 30 minutes to attain adsorption–desorption equilibrium. Fig. 5b shows that the optimum Cr(VI) reduction efficiency (81.5%) was obtained by using NV-2 after 2 h, owing to the lowest recombination rate of charge carriers. NV-2 portrays better Cr(VI) reduction efficiency compared to previous reports, as represented in Table S5. For all synthesized materials, the photocatalytic Cr(VI) reduction followed a pseudo-first order kinetic reaction according to eqn (1):

$$\ln\frac{C_0}{C} = k \quad (1)$$

NV-2 demonstrated a higher rate constant value (k = 1.60) than the others. Furthermore, it was observed that the photocatalytic Cr(VI) reduction was affected by the pH of the reaction medium. The higher reduction efficiency was observed by the NV-2 photocatalyst in acidic medium as compared to basic medium due to the surplus availability of protons. The surface of the NV-2 photocatalyst became positively charged owing to protonation, which promoted the adsorption of $Cr_2O_7^{2-}$ and $HCrO^{4-}$ species, resulting in efficient Cr(VI) reduction. However, the adsorption of $Cr_2O_7^{2-}$ was considerably decreased in basic medium due to the presence of OH^- ions on the surface of the catalyst, lowering the photocatalytic Cr(VI) reduction efficiency of NV-2. Also, the pseudo-first-order kinetics of all the NV samples were comprehensively analysed and are depicted in Fig. 5c. The Cr(VI) reduction efficiency of NV-2 at different pH levels follows pseudo-first-order kinetics, as illustrated in Fig. 5d, which shows the following order: pH 6 > pH 9 > pH 12.[54,55] At an acidic pH, the photocatalyst surface can experience corrosion or deactivation, while at basic pH, the negative charges on both the photocatalyst surface and Cr(VI) causes electrostatic repulsion and reduced adsorption. However, at neutral pH, the optimal balance of charged ions minimizes the surface corrosion. This led to better adsorption of Cr(VI) and efficiently reduced Cr(VI) to Cr(III).[56] The photocatalytic Cr(VI) reduction using NV-2 outperformed previously reported photocatalysts (Fig. 5e and Table S5). The highest photocatalytic activity could be attributed to the higher SSA, surface active sites, and O_v.[57] As displayed in Fig. 5f, reusability tests were performed for up to 10 consecutive cycles. The photocatalytic activity slightly decreased (nearly 27%) after ten cycles due to the loss of catalysts during the recycling experiment.

Proposed mechanism for photocatalytic H_2O_2 generation and Cr(VI) reduction

Based on the above analysis, the possible photocatalytic mechanism for the photocatalytic Cr(VI) reduction and H_2O_2 generation is schematically represented in Fig. 6. In this study, the band structure was analyzed using UV-vis DRS and MS analysis. Visible light induced the formation of e^-–h^+ pairs in the respective CB and VB positions of the NV-2 photocatalyst. M–S analysis verified NV-2 as an n-type semiconductor. The photoinduced h^+ in the VB are not capable of oxidizing water because the VB potential is significantly lower than the required oxidation potential of water (1.76 eV). Furthermore, no H_2O_2 was detected in the experiments, which were carried out in the dark or in the absence of the photocatalyst. The dissolved oxygen underwent direct two-electron reduction pathways to yield H_2O_2 (eqn (2) and (3)).

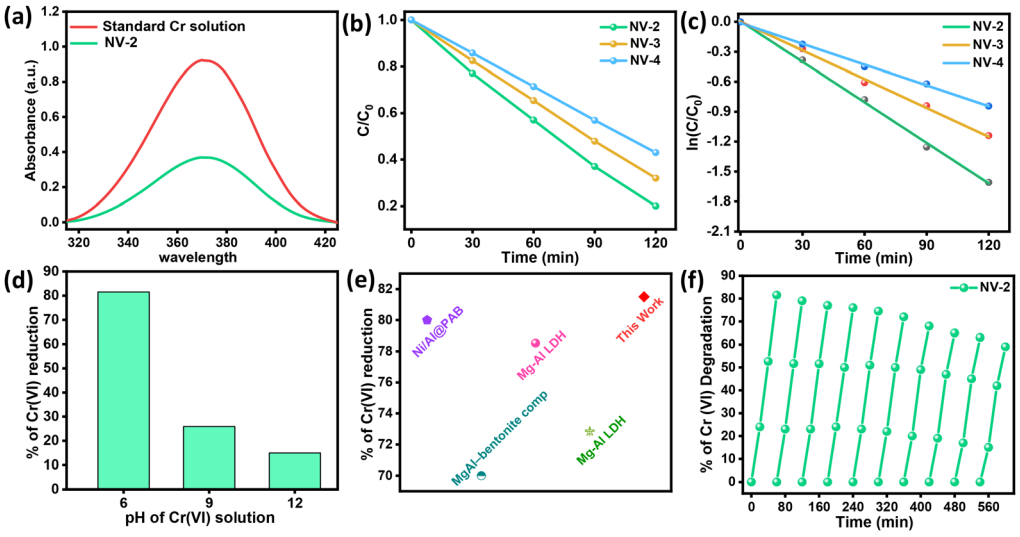

Fig. 5 (a) Photocatalytic Cr(VI) reduction absorbance plot of NV-2 under visible light at various intervals of time. (b) Photocatalytic Cr(VI) reduction absorbance plot of NV-2 under visible light at various intervals of time. (c) Kinetics of the pseudo-first-order mechanism of NV-2. (d) Comparison of the photocatalytic Cr(VI) reduction by NV-2 at different pH values. (e) Comparison of the photocatalytic Cr(VI) reduction by different photocatalysts. (f) Stability testing of the NV-2 catalyst during the Cr(VI) reduction.

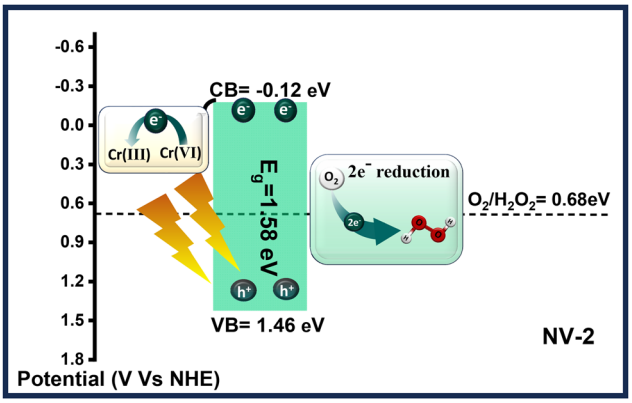

Fig. 6 Schematic illustrating the mechanism of the Cr(VI) reduction using the NV-2 photocatalyst and the direct two-electron pathway of H_2O_2 production.

Two-electron single step/direct H_2O_2 generation:

$$NV \xrightarrow{h\nu} e_{CB}^{-} + h_{VB}^{+} \quad (2)$$

$$O_2 + 2H^+ + 2e^- \rightarrow H_2O_2 \quad (3)$$

The reduction of Cr(VI) could occur under light irradiation because the CB position of NV-2 is more negative than that of the required reduction potential of Cr(VI) (0.33 eV). In parallel, the photoinduced h^+ in the VB of NV-2 facilitated oxidation of alcohol as a sacrificial agent, releasing protons. The scavenger studies confirmed that the photogenerated electrons were primarily used for the reduction of Cr(VI) to Cr(III). The overall photoreduction is summarized in eqn (4) and (5).

$$\text{NV-2} \xrightarrow{h\nu} e^-(CB) + h^+(VB) \quad (4)$$

$$Cr_2O_7^{2-} + 14H^+ + 6e^- \rightarrow 2Cr^{3+} + 7H_2O \quad (5)$$

Conclusion

In summary, this work presents a rational design strategy to address several major challenges in photocatalysis: (i) the incomplete understanding of charge-transfer dynamics and active sites during photocatalytic reactions, (ii) rapid recombination of photoproduced charge carriers, and (iii) poor long-term stability owing to structural degradation under illumination. NiV-LDH nanoflakes were synthesized *via* an eco-friendly reflux method with varying Ni/V ratios. We introduced the surface defect site (O_v) for effective photocatalytic H_2O_2 production for all three photocatalysts and have discussed comparative experiments in detail by employing different parameters. The results reveal that the high SSA due to the O_v of NV-2 facilitates optimized charge carrier separation and surface reaction, which are essential for both H_2O_2 production and Cr(VI) reduction. The elemental, optical and electrochemical characterizations of the synthesized photocatalysts were analyzed. The NV-2 catalyst showed the lowest PL intensity with the highest lifespan and slowest exciton recombination rate, which improved the photocatalytic H_2O_2 production (1152 μmol g^{-1} h^{-1}). Notably, NV-2 exhibited excellent Cr(VI) reduction efficiency of 92% in comparison to other catalysts and was stable for up to 10 cycles. This research work demonstrates a significant pathway for designing high-performance samples in the field of sustainable photocatalysis.

Conflicts of interest

The author declares no competing financial interest.

Data availability

The data supporting this article have been included as part of supplementary information (SI). Supplementary information: chemicals required, material characterisation, photocatalytic H_2O_2 production and Cr(VI) reduction, Williamson–Hall plot, SEM micrograph, colour mapping and EDX pattern of NV-2, particle size distribution analysis, XPS survey spectra, atomic percentage graph of NV-2 photocatalyst, FT-IR spectra, Raman spectra and N_2 adsorption desorption analysis plot, Tauc plot and Urbach energy plot of NV-2, NV-3 and NV-4, comparison of the photocatalytic H_2O_2 decomposition of the NV-2 photocatalyst and pure H_2O_2, XRD plot of NV-2 after photocatalysis, and comparison of photocatalytic H_2O_2 productions (Table S4, PDF). See DOI: https://doi.org/10.1039/d5dt02178b.

Acknowledgements

The authors are very much thankful to SOA (Deemed to be University) management for their support and encouragement.

References

1 H. Tong, J. Odutola, J. Song, L. Peng, N. Tkachenko, M. Antonietti and C. M. Pelicano, Boosting the quantum efficiency of ionic carbon nitrides in photocatalytic H_2O_2 evolution via controllable n→ π* electronic transition activation, *Adv. Mater.*, 2024, **36**, 2412753.
2 K. S. Ranjith, D. R. Kumar, S. M. Ghoreishian, Y. S. Huh, Y. K. Han and R. R. Kumar, A radially controlled ZnS interlayer on ultra-long ZnO–Gd_2S_3 core–shell nanorod arrays for promoting the visible photocatalytic degradation of antibiotics, *Nanoscale*, 2020, **12**, 14047–14060.
3 J. Sahu, J. Panda, P. P. Sarangi and K. Parida, Boosting the Photocatalytic O_2 Reduction Reaction for H_2O_2 production over CuS Nanosheets decorated with CdSe Quantum dots, *ChemCatChem*, 2025, **17**, 202402147.
4 S. M. Ghoreishian, K. S. Ranjith, M. Ghasemi, B. Park, S. K. Hwang, N. Irannejad, M. Norouzi, S. Y. Park, R. Behjatmanesh-Ardakani, S. M. Pourmortazavi and S. Mirsadeghi, Engineering the photocatalytic performance

of B-C_3N_4@ Bi_2S_3 hybrid heterostructures for full–spectrum–driven Cr(VI) reduction and *in situ* H_2O_2 generation: Experimental and DFT studies, *Chem. Eng. J.*, 2023, **452**, 139435.

5 S. M. Ghoreishian, K. S. Ranjith, B. Park, S. K. Hwang, R. Hosseini, R. Behjatmanesh-Ardakani, S. M. Pourmortazavi, H. U. Lee, B. Son, S. Mirsadeghi and Y. K. Han, Full-spectrum-responsive Bi_2S_3@ CdS S-scheme heterostructure with intimated ultrathin RGO toward photocatalytic Cr(VI) reduction and H_2O_2 production: Experimental and DFT studies, *Chem. Eng. J.*, 2021, **419**, 129530.

6 Y. Teng, X. M. Zhang, R. L. Zhu, S. Chen, M. Y. Xie, K. Wu, Q. P. Tian, X. Y. Wang, Z. Wu, J. L. Ma and L. Sun, Interface–Engineered C_4N/MgAl–LDH Heterostructure for High–Performance Photocatalytic H_2O_2 Production, *Angew. Chem.*, 2025, 202516296.

7 H. S. Chavan, C. H. Lee, A. I. Inamdar, J. Han, S. Park, S. Cho, N. K. Shreshta, S. U. Lee, B. Hou, H. Im and H. Kim, Designing and tuning the electronic structure of nickel–vanadium layered double hydroxides for highly efficient oxygen evolution electrocatalysis, *ACS Catal.*, 2022, **12**, 3821–3831.

8 K. Zeng, M. Chao, M. Tian, S. Jiang, Y. Zhaoshi, J. Feng, Z. Sun and Y. Li, Optimizing d–p Orbital Hybridization with Abundant Unfilled Antibonding Orbital in Multi–Metal Layered Double Hydroxide: Motivating Efficient Oxygen Evolving, *Adv. Funct. Mater.*, 2024, **34**, 2315080.

9 A. Sheik, K. S. Ranjith, S. M. Ghoreishian, Y. Yang, Y. Park, S. Son, Y. K. Han and Y. S. Huh, Green approach for the fabrication of dual-functional S/N doped graphene tagged ZnO nanograins for in vitro bioimaging and water pollutant remediation, *Environ. Pollut.*, 2024, **343**, 123077.

10 S. Mirsadeghi, S. M. Ghoreishian, H. Zandavar, R. Behjatmanesh-Ardakani, E. Naghian, M. Ghoreishian, A. Mehrani, N. Abdolhoseinpoor, M. R. Ganjali, Y. S. Huh and S. M. Pourmortazavi, In-depth insight into the photocatalytic and electrocatalytic mechanisms of $Mg_3V_2O_8$@ $Zn_3V_2O_8$@ ZnO ternary heterostructure toward linezolid: Experimental and DFT studies, *J. Environ. Chem. Eng.*, 2023, **11**, 109106.

11 J. Sahu, S. Mansingh, B. P. Mishra, D. Prusty and K. Parida, compositionally engineered Cd–Mo–Se alloyed QDs toward photocatalytic H_2O_2 production and Cr(vi) reduction with a detailed mechanism and influencing parameters, *Dalton Trans.*, 2023, **52**, 16525–16537.

12 D. P. Sahoo, K. K. Das, S. Mansingh, S. Sultana and K. Parida, Recent progress in first row transition metal Layered double hydroxide (LDH) based electrocatalysts towards water splitting: A review with insights on synthesis, *Coord. Chem. Rev.*, 2022, **469**, 214666.

13 W. A. Qureshi, S. N. U. Z. Haider, R. N. Ali, A. Naveed, S. Khan, M. A. Qaiser, A. Ali, R. Wahab, A. A. Al-Khedhairy, R. Shaosheng and L. Wang, Room temperature preparation of novel g-C_3N_4/RuNP/ZIF-8 Z-scheme heterojunction for solar-light driven H_2 generation, *Int. J. Hydrogen Energy*, 2024, **77**, 808–816.

14 W. A. Qureshi, S. N. U. Z. Haider, A. Naveed, A. Ali, Q. Liu and J. Yang, Recent progress in the synthesis, characterization and photocatalytic application of energy conversion over single metal atoms decorated graphitic carbon nitride, *Int. J. Hydrogen Energy*, 2023, **48**, 19459–19485.

15 S. N. U. Z. Haider, W. A. Qureshi, R. N. Ali, R. Shaosheng, A. Naveed, A. Ali, M. Yaseen, Q. Liu and J. Yang, Contemporary advances in photocatalytic CO_2 reduction using single-atom catalysts supported on carbon-based materials, *Adv. Colloid Interface Sci.*, 2024, **323**, 103068.

16 D. P. Sahoo, S. Patnaik and K. Parida, An amine functionalized ZnCr-LDH/MCM-41 nanocomposite as efficient visible light induced photocatalyst for Cr(VI) reduction, *Mater. Today: Proc.*, 2021, **35**, 252–257.

17 W. A. Qureshi, S. N. U. Z. Haider, M. A. Qaiser, S. Khan, W. Wang, R. N. Ali, A. Ali, A. Naveed, M. H. Abdurahman, M. U. Khan and M. Tayyab, Breakthrough in Plasmonic Enhanced MOFs: Design, Synthesis, and Catalytic Mechanisms for Various Photocatalytic Applications, *Environ. Res.*, 2025, 121257.

18 F. E. B. Coelho, V. M. Candelario, E. M. R. Araújo, T. L. S. Miranda and G. Magnacca, Photocatalytic, reduction of Cr(VI) in the presence of humic acid using immobilized Ce–ZrO_2 under visible light, *Nanomaterials*, 2020, **10**, 779.

19 Y. Liu, X. Du and Z. Huang, Photocatalytic reduction of aqueous chromium(VI) by RuO_2/g-C_3N_4 composite under visible light irradiation, *RSC Adv.*, 2025, **15**, 16724–16733.

20 J. Liang, C. Jing, J. Wang and Y. Men, Photocatalytic reduction of Cr(VI) over g-C_3N_4 photocatalysts synthesized by different precursors, *Molecules*, 2021, **26**, 7054.

21 P. Prabha Sarangi, D. Prava Sahoo, U. Aparajita Mohanty, S. Nayak and K. Parida, Recent advancement in quantum dot modified layered double hydroxide towards photocatalytic, electrocatalytic, and photoelectrochemical applications, *ChemCatChem*, 2024, **16**, 202301533.

22 D. Jiao, C. Ding, M. Xu, X. Ruan, S. K. Ravi and X. Cui, Modulating yeager adsorption configuration of O_2 through Cd doping in $Zn_3In_2S_6$ for photosynthesis of H_2O_2, *Adv. Funct. Mater.*, 2025, **35**, 2416753.

23 Y. Hu, T. Shen, Z. Wu, Z. Song, X. Sun, S. Hu and Y. F. Song, Coordination stabilization of Fe by porphyrin–intercalated NiFe–LDH under industrial–level alkaline conditions for long–term electrocatalytic water oxidation, *Adv. Funct. Mater.*, 2025, **35**, 2413533.

24 K. S. Ranjith, R. Maleki, S. M. Ghoreishian, A. Mohammadi, G. S. R. Raju, Y. S. Huh and Y. K. Han, Defective phase engineering of S-scheme TiO_2–SnS/SnS_2 core–shell photocatalytic nanofibers for elevated visible light responsive H 2 generation and nitrogen fixation, *J. Mater. Chem. A*, 2024, **12**, 33818–33833.

25 G. Li, Y. Xu, H. Pan, X. Xie, R. Chen, D. Wu and L. Wang, A bimetallic synergistic effect on the atomic scale of defect-enriched NiV-layered double hydroxide nanosheets for

electrochemical phenol hydroxylation, *J. Mater. Chem. A*, 2022, **10**, 6748–6761.

26 A. Karmakar, K. Karthick, S. S. Sankar, S. Kumaravel, R. Madhu, K. Bera, H. N. Dhandapani, S. Nagappan, P. Murugan and S. Kundu, Stabilization of ruthenium nanoparticles over NiV-LDH surface for enhanced electrochemical water splitting: an oxygen vacancy approach, *J. Mater. Chem. A*, 2022, **10**, 3618–3632.

27 A. De, R. Madhu, K. Bera, H. N. Dhandapani, S. Nagappan, S. S. Roy and S. Kundu, Deciphering the amplification of dual catalytic active sites of Se-doped NiV LDH in water electrolysis: a hidden gem exposure of anion doping at the core-lattice LDH framework, *J. Mater. Chem. A*, 2023, **11**, 25055–25071.

28 M. Taha, S. Walia, T. Ahmed, D. Headland, W. Withayachumnankul, S. Sriram and M. Bhaskaran, Insulator–metal transition in substrate-independent VO_2 thin film for phase-change devices, *Sci. Rep.*, 2017, **7**, 17899.

29 S. Wang, J. Zhu, T. Li, F. Ge, Z. Zhang, R. Zhu, H. Xie and Y. Xu, Oxygen vacancy-mediated CuCoFe/Tartrate-LDH catalyst directly activates oxygen to produce superoxide radicals: transformation of active species and implication for nitrobenzene degradation, *Environ. Sci. Technol.*, 2022, **56**, 7924–7934.

30 Y. Yan, J. Lin, T. Xu, B. Liu, K. Huang, L. Qiao, S. Liu, J. Cao, S. C. Jun, Y. Yamauchi and J. Qi, Atomic–level platinum filling into Ni–vacancies of dual–deficient NiO for boosting electrocatalytic hydrogen evolution, *Adv. Energy Mater.*, 2022, **12**, 2200434.

31 D. Wang, Q. Li, C. Han, Q. Lu, Z. Xing and X. Yang, Atomic and electronic modulation of self-supported nickel-vanadium layered double hydroxide to accelerate water splitting kinetics, *Nat. Commun.*, 2019, **10**, 3899.

32 A. De, R. Madhu, K. Bera, H. N. Dhandapani, S. Nagappan, S. S. Roy and S. Kundu, Deciphering the amplification of dual catalytic active sites of Se-doped NiV LDH in water electrolysis: a hidden gem exposure of anion doping at the core-lattice LDH framework, *J. Mater. Chem. A*, 2023, **11**, 25055–25071.

33 Z. Wu, S. Bai, T. Shen, G. Liu, Z. Song, Y. Hu, X. Sun, L. Zheng and Y. F. Song, Ultrathin NiV Layered Double Hydroxide for Methanol Electrooxidation: Understanding the Proton Detachment Kinetics and Methanol Dehydrogenation Oxidation, *Small*, 2024, **20**, 2307975.

34 D. J. Lockwood, D. Bertrand, P. Carrara, G. Mischler, D. Billerey and C. Terrier, Raman spectrum of NiCl2, *J. Phys. C: Solid State Phys.*, 1979, **12**, 3615.

35 X. Tang, C. Yu, J. Zhang, K. Liu, D. Zeng, F. Li, G. Ma, Y. Jiang and Y. Zhu, Furan-based HTCC/In_2S_3 heterojunction achieves fast charge separation to boost the photocatalytic generation of H_2O_2 in pure water, *ACS Catal.*, 2024, **14**, 16245–16255.

36 K. T. Keyser, V. Wotring, C. E. Strang and J. P. Stein, *The role of acetylcholine and its receptors in retinal processing*, Elsevier, 2017, *Ref. Mod. Neurosci. Biobehav. Psych*.

37 D. Prusty, S. Mansingh, N. Priyadarshini and K. M. Parida, Defect control via compositional engineering of Zn-Cu-In-S alloyed QDs for photocatalytic H_2O_2 generation and micropollutant degradation: affecting parameters, kinetics, and insightful mechanism, *Inorg. Chem.*, 2022, **61**, 18934–18949.

38 H. Hu, X. Li, K. Zhang, G. Yan, W. Kong, A. Qin, Y. Ma, A. Li, K. Wang, H. Huang and X. Sun, Dual Modification of Metal–Organic Frameworks for Exceptional High Piezo–Photocatalytic Hydrogen Production, *Adv. Mater.*, 2025, **37**, 2419023.

39 X. Liu, Y. Li, J. Zhang and J. Lu, Ultrathin Ni/V-layered double hydroxide nanosheets for efficient visible-light-driven photocatalytic nitrogen reduction to ammonia, *Nano Res.*, 2021, **14**, 3372–3378.

40 J. Hou, K. Wang, X. Zhang, Y. Wang, H. Su, C. Yang, X. Zhou, W. Liu, H. Hu, J. Wang and C. Li, Synergistic Defect Sites and CoO_x Nanoclusters in Polymeric Carbon Nitride for Enhanced Photocatalytic H_2O_2 Production, *ACS Catal.*, 2024, **14**, 10893–10903.

41 H. Li, J. Li, Z. Ai, F. Jia and L. Zhang, Oxygen Vacancy Mediated Photocatalysis of BiOCl: Reactivity, Selectivity, and Perspectives, *Angew. Chem., Int. Ed.*, 2018, **57**, 122–138.

42 H. Zhang, C. Li, L. Lyu and C. Hu, Surface oxygen vacancy inducing peroxy mono sulfate activation through electron donation of pollutants over cobalt-zinc ferrite for water purification, *Appl. Catal., B*, 2020, **270**, 118874.

43 M. Li, J. Wang and Z. Jin, In Situ X-ray Photoelectron Spectroscopy (XPS) Demonstrated Graphdiyne (gC_nH_{2n-2}) Based GDY-CuI/NiV-LDH Double S-Scheme Heterojunction for Efficient Photocatalytic Hydrogen Evolution, *Energy Fuels*, 2023, **37**, 5399–5411.

44 J. An, M. Ruan, Y. Xue, D. Tian, Z. Fang and L. Li, Facile Carburization Engineering to Construct Porous Locally Carbonized MoO_3 Composite with Long-Term Stable Lithium Storage Capacity, *ACS Appl. Energy Mater.*, 2025, **8**, 1041–1050.

45 Y. Li, Z. Pei, D. Luan and X. W. D. Lou, Triple-phase photocatalytic H_2O_2 production on a Janus fiber membrane with asymmetric hydrophobicity, *J. Am. Chem. Soc.*, 2024, **146**, 3343–3351.

46 X. Liu, Y. Li, J. Zhang and J. Lu, Ultrathin Ni/V-layered double hydroxide nanosheets for efficient visible-light-driven photocatalytic nitrogen reduction to ammonia, *Nano Res.*, 2021, **14**, 3372–3378.

47 X. Tang, C. Yu, J. Zhang, K. Liu, D. Zeng, F. Li, F. Li, G. Ma, Y. Jiang and Y. Zhu, Furan-based HTCC/In_2S_3 heterojunction achieves fast charge separation to boost the photocatalytic generation of H_2O_2 in pure water, *ACS Catal.*, 2024, **14**, 16245–16255.

48 J. Zhao, L. Wang, T. Zhou, Y. Yan, J. Sun, B. Hu, B. Liu, C. Liu and G. Che, Molecularly Tunable Donor–Acceptor Integrated Carbon Nitride for Sunlight–Driven H_2O_2 Synthesis: Mechanism and Performance Insights, *Small*, 2025, **21**, 2500679.

49 P. Das, J. Roeser and A. Thomas, Solar light driven H_2O_2 production and selective oxidations using a covalent organic framework photocatalyst prepared by a multicomponent reaction, *Angew. Chem.*, 2023, **135**, 202304349.
50 L. Wang, B. Li, D. D. Dionysiou, B. Chen, J. Yang and J. Li, Overlooked formation of H_2O_2 during the hydroxyl radical-scavenging process when using alcohols as scavengers, *Environ. Sci. Technol.*, 2022, **56**, 3386–3396.
51 D. Wang, W. Zhao, F. Tan, X. Wang, J. Dong, S. Zhou, G. Liu and P. Gu, . Selective Oxygen Activation by Integrating Dual Photosensitizers in Conjugated Porous Polymers and Microenvironments Manipulation for High–Performance Water Purification and H_2O_2 Production, *Adv. Funct. Mater.*, 2025, **35**, 2419010.
52 W. Zeng, Y. Dong, X. Ye, Y. Zhao, Z. Zhang, T. Zhang, L. Zhang, J. Chen and X. Guan, Modulating Local Proton Coverage and* OOH Generation via Coupled Multiple Sites for Enhanced Photocatalytic H_2O_2 Production, *ACS Catal.*, 2025, **15**, 6036–6045.
53 J. Y. Yue, Z. X. Pan, R. Z. Zhang, Q. Xu, P. Yang and B. Tang, One–Pot Synthesis of Fully Conjugated Covalent Organic Frameworks via the Pictet–Spengler Reaction for Boosting H_2O_2 Photogeneration in Real Seawater, *Adv. Funct. Mater.*, 2025, **35**, 2421514.
54 B. Ou, J. Wang, Y. Wu, S. Zhao and Z. Wang, . Efficient removal of Cr(VI) by magnetic and recyclable calcined CoFe-LDH/g-C_3N_4 via the synergy of adsorption and photocatalysis under visible light, *Chem. Eng. J.*, 2020, **380**, 122600.
55 J. He, L. Liu, N. Fu, Y. Zhao, L. Zhang, L. Feng, G. Teng, X. Li and C. Zhang, Construction of Sulfur-Vacancy-Modified 0D/2D S-Scheme Heterojunction for Enhancing Photocatalytic Cr(VI) Reduction, *ACS Mater. Lett.*, 2025, **7**, 566–575.
56 M. Shirzad Siboni, M. T. Samadi, J. K. Yang and S. M. Lee, Photocatalytic reduction of Cr(VI) and Ni(II) in aqueous solution by synthesized nanoparticle ZnO under ultraviolet light irradiation: a kinetic study, *Environ. Technol.*, 2011, **32**, 1573–1579.
57 K. K. Das, U. A. Mohanty, L. Paramanik, D. P. Sahoo and K. Parida, Facile fabrication of B-rGO/$ZnFe_2O_4$ p–n heterojunction-based S-scheme exciton engineering for photocatalytic Cr(vi) reduction: kinetics, influencing parameters and detailed mechanism, *RSC Adv.*, 2024, **14**, 20312–20327.

